ISSN 1674-1056
http://cpb.iphy.ac.cn
http://iopscience.iop.org/cpb
中国物理 B
Chinese Physics
中国物理 Chinese Physics B

# Simulation of a torrential rainstorm in Xinjiang and gravity wave analysis

Rui Yang(杨瑞), YiLiu(刘毅), Ling-Kun Ran(冉令坤), Yu-Li Zhang(张玉李)
**Citation:**Chin. Phys. B . 2018, 27(5): 059201. **doi:** 10.1088/1674-1056/27/5/059201

Journal homepage: http://cpb.iphy.ac.cn; http://iopscience.iop.org/cpb

**What follows is a list of articles you may be interested in**

---

## Spatiotemporal distribution characteristics and attribution of extreme regional low temperature event

Feng Tai-Chen, Zhang Ke-Quan, Su Hai-Jing, Wang Xiao-Juan, Gong Zhi-Qiang, Zhang Wen-Yu
Chin. Phys. B . 2015, 24(10): 109201. **doi:** 10.1088/1674-1056/24/10/109201

## Objective identification research on cold vortex and mid-summer rainy periods in Northeast China

Gong Zhi-Qiang, Feng Tai-Chen, Fang Yi-He
Chin. Phys. B . 2015, 24(4): 049204. **doi:** 10.1088/1674-1056/24/4/049204

## An approach to estimating and extrapolating model error based on inverse problem methods: towards accurate numerical weather prediction

Hu Shu-Juan, Qiu Chun-Yu, Zhang Li-Yun, Huang Qi-Can, Yu Hai-Peng, Chou Ji-Fan
Chin. Phys. B . 2014, 23(8): 089201. **doi:** 10.1088/1674-1056/23/8/089201

## Three-dimensional spiral structure of tropical cyclone under four-force balance

Liu Shi-Kuo, Fu Zun-Tao, Liu Shi-Da
Chin. Phys. B . 2014, 23(6): 069201. **doi:** 10.1088/1674-1056/23/6/069201

## Predicting extreme rainfall over eastern Asia by using complex networks

He Su-Hong, Feng Tai-Chen, Gong Yan-Chun, Huang Yan-Hua, Wu Cheng-Guo, Gong Zhi-Qiang
Chin. Phys. B . 2014, 23(5): 059202. **doi:** 10.1088/1674-1056/23/5/059202

---

# Simulation of a torrential rainstorm in Xinjiang and gravity wave analysis*

Rui Yang(杨瑞)[1,2], Yi Liu(刘毅)[1], Ling-Kun Ran(冉令坤)[1,†], and Yu-Li Zhang(张玉李)[1]

[1] *Institute of Atmospheric Physics, Chinese Academy of Sciences, Beijing* 100029, *China*
[2] *University of Chinese Academy of Sciences, Beijing* 100049, *China*

(Received 29 September 2017; revised manuscript received 21 December 2017; published online 26 April 2018)

We used a weather research and forecasting model to simulate a torrential rainstorm that occurred in Xinjiang, China during June 16–17, 2016. The model successfully simulated the rainfall area, precipitation intensity, and changes in precipitation. We identified a clear wave signal using the two-dimensional fast Fourier transform method; the waves propagated westwards, with wavelengths of 45–20 km, periods of 50–120 min, and phase velocities mainly concentrated in the −25 m/s to −10 m/s range. The results of wavelet cross-spectral analysis further confirmed that the waves were gravity waves, peaking at 11:00 UTC, June 17, 2016. The gravity wave signal was identified along 79.17–79.93°E, 81.35–81.45°E and 81.5–81.83°E. The gravity waves detected along 81.5–81.83°E corresponded well with precipitation that accumulated in 1 h, indicating that gravity waves could be considered a rainstorm precursor in future precipitation forecasts.

**Keywords:** gravity wave, rainstorm, spectral analysis methods, weather research and forecasting model

**PACS:** 92.60.–e, 92.60.Wc, 92.60.jf **DOI:** 10.1088/1674-1056/27/5/059201

## 1. Introduction

Gravity waves are ubiquitous in the atmosphere, and play an important role in the transport of momentum and energy between the troposphere and stratosphere.[1] Several reasons have been proposed to explain the excitation of gravity waves including topography. The generation of Lee waves or mountain waves by airflow over a mountain occurs at scales between 10 km and 100 km, corresponding well with the size of the mountains.[2] The generation of gravity waves is accompanied by geostrophic adjustment, in which air adjusts from non-equilibrium flow to equilibrium flow and the momentum, energy and potential vorticity are redistributed, generating gravity waves and releasing unstable energy. The evolution of the jet-front systems is typical in gravity waves generated through geostrophic adjustment. Uccellini and Koch[3] proposed a conceptual model that located the activity region of gravity waves at the north of the surface front and the east of the upper jet, and determined their phase velocity by the speed of the jet-front system.[4] Simulations further confirmed that the gravity wave sources were located at the front of the ridge line at high latitudes and in the vicinity of the trough at mid-latitudes.[5] The authors concluded that water vapor played a crucial role in the excitation of gravity waves such that wet sources of gravity waves could produce wider power spectra, wavelength spectra and phase velocity spectra than dry sources of gravity waves.[6,7] Wind shear has also been widely discussed as a source of gravity waves through the envelope radiation mechanism and nonlinear Kelvin–Helmholtz instability.[8,9] The role of the wave–wave interaction as a gravity wave generator has also been studied; the parametric subharmonic instability has been used to interpret the generation of gravity waves and these findings were supported by radar observations.[10] Convection systems are another important source of gravity waves that has been widely studied. Three mechanisms are currently used to interpret the generation of gravity waves by convection: the obstacle effect,[11] the mechanical oscillator effect[12] and pure thermal forcing.[13] Some studies have also attempted to interpret the sources of gravity waves using wave equations, and the results showed that latent heating was predominant in the generation of gravity waves.[14,15]

Convection can not only generate gravity waves but also acquire feedback, which can help to form new convection cells. The wave-conditional instability of the second kind (CISK) mechanism has been widely used to explain the interaction between gravity waves and convection;[16,17] however, the calculation of spreading speeds based on this mechanism generally disagrees with the observations.[18] A combination of wave ducting and the wave-CISK mechanism has successfully explained the propagation and maintenance of convection systems.[19,20] Subsequently, many studies have focused on the effects of gravity waves on convection; for example, Liu *et al.*[21] investigated the role of gravity waves in the development of squall lines and found that a combination of gravity waves and cold pool outflow maintained the propagation and development of squall lines. Su and Zhai[22] discovered us-

*Project supported by China Special Fund for Meteorological Research in the Public Interest (Grant No. GYHY201406002), the National Natural Science Foundation of China (Grant Nos. 41575065 and 41405049), the National Natural Science Foundation International Cooperation Project, China (Grant No. 41661144024), and Strategic Priority Research Program of Chinese Academy of Sciences (Grant No. XDA17010100).

†Corresponding author. E-mail: rlk@mail.iap.ac.cn

© 2018 Chinese Physical Society and IOP Publishing Ltd 

ing high-resolution numerical models that gravity waves and convergence lines together promoted convection initiation.

Considering the close correlation between gravity waves and convection, quantitative analysis of the parameters of gravity waves and the spatiotemporal characteristics of wave parameters have become an essential work in this field. The polarization property of the perturbation quantities of horizontal wind fields is key to extracting the parameters of inertial gravity waves (IGWs). Using this property in horizontal wind fields, Thompson[23] introduced rotary spectral analysis, based on Fourier transform, to analyze the vertical propagation of gravity waves. The disadvantage of this method is that it cannot be used to obtain the horizontal propagation direction or frequencies of gravity waves. Cot and Barat[24] attempted to extract the horizontal and vertical propagation directions of gravity waves and calculated wave frequencies using the hodograph method; however, the results were inaccurate when multiple waves were simultaneously present in the hodographs. The cross-spectral method combines the advantages of the rotary spectral analysis and the hodograph method,[25] and has therefore been widely adopted. However, the cross-spectral method cannot be used to obtain the spatiotemporal evolution characteristics of wave parameters. To solve this problem, Lu *et al.*[26] combined the continuous wavelet transform and cross-spectral methods based on the polarization of gravity waves, and successfully extracted the temporal and spatial characteristics of gravity waves from the observed data. Due to the presence of noise, wave signals extracted from the observed data might be false waves; significant tests in the wavelet power spectrum analysis and wavelet cross-spectral analysis should be used to improve the gravity wave analysis.[27,28]

In summary, the wavelet cross-spectral method makes it possible to acquire the spatiotemporal characteristics of gravity waves, but studies on this method have mainly focused on horizontal wind fields (i.e., $u$ and $v$ directions), whereas studies using the spectral analysis method based on the gravity wave model have ignored the geostrophic parameter $f$. For modeling mesoscale IGWs, the geostrophic parameter must not be neglected, and the fixed-phase polarization relationship between $m\pi$ in the $u$ and $v$ horizontal wind fields in the pure gravity wave model does not exist for IGWs.[29] Gravity wave identification and spectral analysis have only been applied to observations. Application of the spectral analysis methods in weather research and forecasting (WRF) models to study gravity waves would be helpful in identifying gravity waves with smaller wavelengths than typically observed. Spectral analysis would also permit the identification of quantitative gravity wave parameters in higher-resolution mesh regions than possible in isolated sounding observation stations.

Therefore, we used the three-dimensional (3D) inertial gravity wave model and the phase polarization relationship between $\pi/2$ of the horizontal divergence and vertical vorticity to identify gravity waves and analyze their spatiotemporal characteristics during a torrential rainstorm that occurred in Xinjiang, China duirng June 16–17, 2016.

## 2. Data and methods

The data used in this paper included China merged analysis hourly precipitation data, global forecast system (GFS) data at a resolution of 0.25°, and WRF3.7.1 model output at a resolution of 3 km. Fast Fourier transformation (FFT), cross-spectral analysis, wavelet spectral analysis, and inverse FFT (IFFT) were used to analyze the gravity waves based on their polarization property.

## 3. Observed precipitation and circulation background

### 3.1. Observed precipitation

A torrential rainstorm occurred in Xinjiang, China during June 16–17, 2016. Precipitation was mainly concentrated in Yili Valley and distributed along the Borohoro Mountains from the northwest to southeast (Fig. 1). Xinjiang, the largest province in China, has an extensive variety of landforms given its uneven topography. Xinjiang contains few meteorological observation stations; thus, there is apparent discontinuity in the precipitation zone shown in Fig. 1. Heavy rainfall (over 48 mm within 24 h) mainly occurred in Nilka County and Gongliu County, and to a lesser extent in Yining County, Turks County, Xinyuan County, and Huocheng County. The maximum rainfall was recorded in the boundary area between Yining County and Nilka County, with a 24 h accumulated rainfall of more than 96 mm, defining a torrential rainstorm based on the local operational standard set by Xinjiang Province. This rainstorm was characterized by high intensity, concentrated location, and spatial and temporal inhomogeneity, indicating that it was a typical mesoscale weather process.

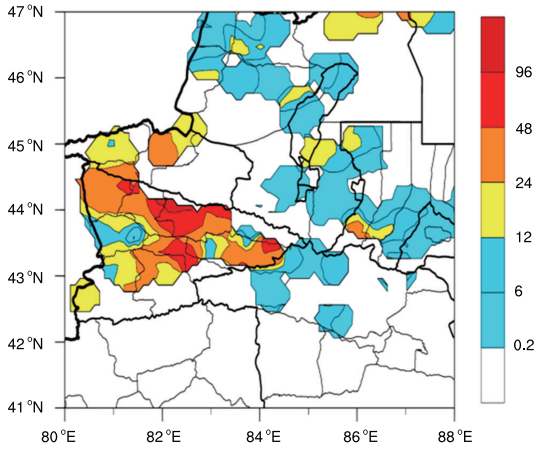



**Fig. 1.** Observed 24 h accumulated precipitation (mm) from 12:00 UTC, June 16, 2016 to 12:00 UTC, June 17, 2016.

### 3.2. Synoptic background

During the rainstorm, a South Asian high increasingly strengthened and moved westwards, with a high-pressure center stably maintained over the Tibetan Plateau (Figs. 2(a) and 2(d)). At the same time, a high-level trough and the South Asian high increased the speed of the upper-level jet stream, with Yili Valley to the left of the exit of the upper-level jet stream. The divergence to the left of the exit of the upper-level jet stream at 200 hPa promoted convergence on the surface at Yili Valley. The synoptic background at 500 hPa (Figs. 2(b) and 2(e)) exhibited the classic weather pattern of two troughs and one ridge; one trough was located to the west of Lake Balkhash and the other was over northeastern China, extending from the northeast China cold vortex to the Changjiang-Huaihe basin, with the ridge situated over Lake Baikal. The trough to the west of Lake Balkhash gradually developed into a cold vortex to the west of Xinjiang, such that Xinjiang was under the control of the southwesterly flow in front of the trough. Under these favorable weather conditions, a cyclonic circulation formed to the west of Yili Valley (Figs. 2(c) and 2(f)). The northwesterly flow around Lake Balkhash steered the cold air in Siberia southwards. When the cold air reached Central Asia, it turned right and entered Yili Valley along the North Tianshan basin, providing sufficient moisture to promote the development of the torrential storm in the Yili Valley area of Xinjiang Province.

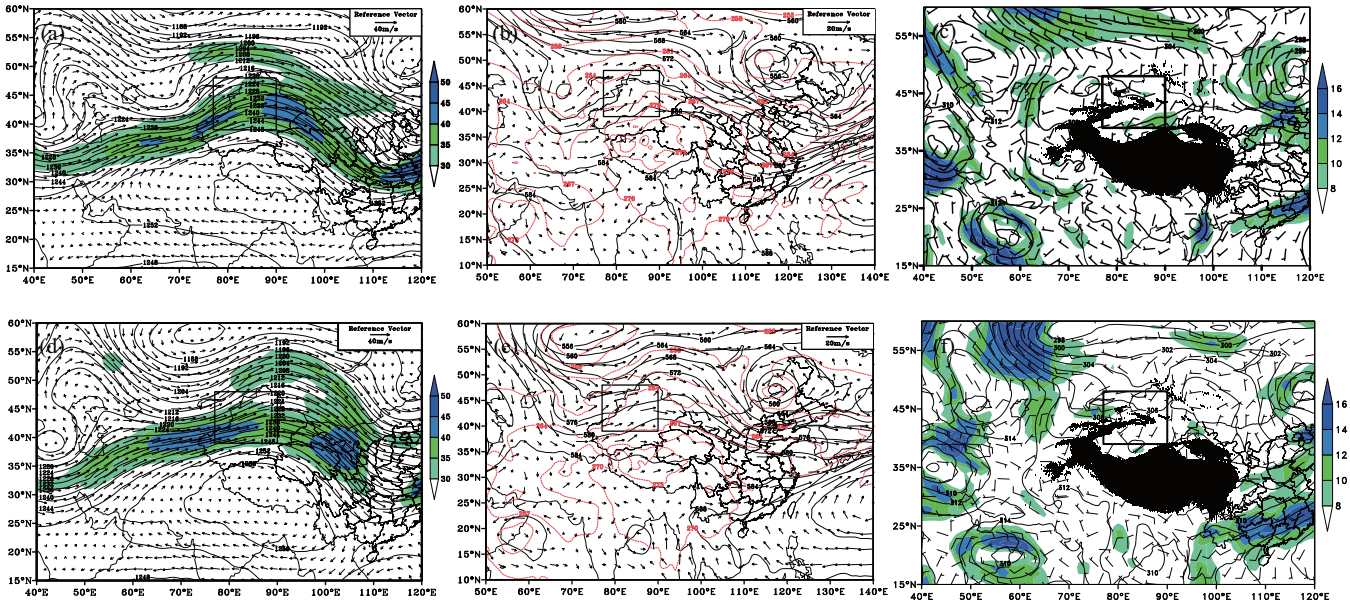



**Fig. 2.** Upper, middle and lower-level synoptic weather patterns at (a)–(c) 12:00 UTC, June 16, 2016 and (d)–(f) 06:00 UTC, June 17, 2016, respectively. (a), (d) Geopotential height (solid lines, dagpm) and wind speed $\geq$ 30 m/s (vectors, m/s) at 200 hPa; (b), (e) geopotential height (solid lines, dagpm), temperature (dashed lines, °C), and wind speed (vectors, m/s) at 500 hPa; (c), (f) geopotential height (solid lines, dagpm), wind speed (barbed lines, knots), and wind speed $\geq$ 8 m/s (shaded areas, m/s) at 700 hPa; the rectangular area represents the domain of the simulation area.

### 3.3. Water vapor condition

The water vapor originated mainly from the Arctic Ocean (Fig. 3(a)). Northerly flows to the east of the arctic high transported the water vapor southwards to Western Siberia. The water vapor was driven by the northerly flow to the east of the Ural high pressure zone to move southwards into Kazakhstan, then turned right and entered Yili Valley along the North Tianshan basin where the water vapor converged at last with the maximum absolute value of water vapor flux divergence, which exceeded $5 \times 10^{-7}$ g·cm$^{-2}$·s$^{-1}$·hPa$^{-1}$. The convergent water vapor was forcedly uplifted by the steep terrain,

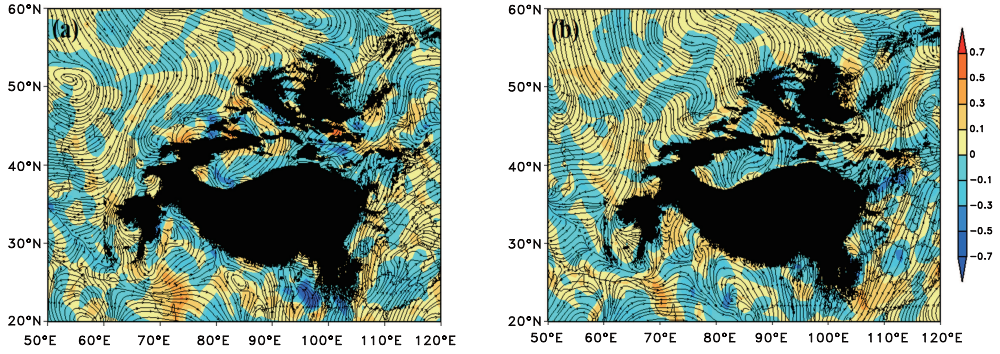



**Fig. 3.** Water vapor flux (streamlines, g·cm$^{-1}$·s$^{-1}$·hPa$^{-1}$) and water vapor flux divergence (shaded areas, $10^{-7}$g·cm$^{-2}$·s$^{-1}$·hPa$^{-1}$) at (a) 18:00 UTC, June 16, 2016; and (b) 12:00 UTC, June 17, 2016.

and water vapor in the atmosphere further condensed into rainwater, finally leading to the occurrence of the torrential rainstorm. At 12:00 UTC, June 17 (Fig. 3(b)), the convergence of water vapor in Yili Valley significantly weakened, and the convergence center moved northeastwards to Altay Prefecture, then the heavy rains in Yili Valley gradually decreased.

## 4. Numerical simulation and model verification

### 4.1. Model description

We used the WRF model version 3.7.1 to simulate the torrential storm with a single domain with $539 \times 384$ grid points in the north-south and east-west directions, and a horizontal grid spacing of 3 km. The simulation was performed for the storm occurring over a period of 48 h, from 00:00 UTC, June 16, 2016 to 00:00 UTC, June 18, 2016. The initial and boundary conditions were derived from the National Centers for Environmental Prediction/National Center for Atmospheric Research (NCEP/NCAR) GFS reanalysis dataset, with a resolution of $0.25^\circ \times 0.25^\circ$. The main parameterizations used in the model are as follows: a microphysics scheme with ice, snow and graupel processes suitable for high-resolution simulation (Thompson); a boundary scheme from the asymmetric convective model with a non-local upward mixing and local downward mixing closure scheme (ACM2); a two-layer scheme from the Pleim–Xiu land surface model with vegetation and sub-grid tiling (PX LSM); a longwave radiation scheme from the rapid radiative transfer model (RRTM). The model was set up to provide output every 10 min. The simulation area and topographic distribution are presented in Fig. 4 (red line indicates the cross-section referred to below).

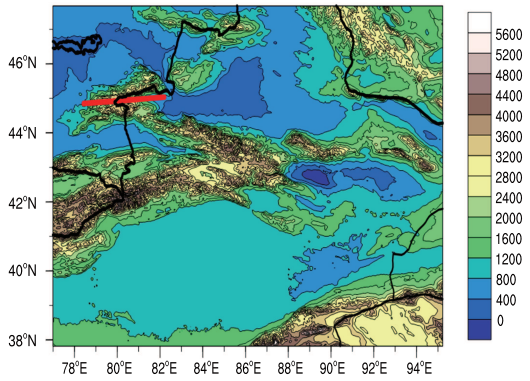



**Fig. 4.** Terrain height (in units of m) in the numerical simulation domain. Red line indicates the cross-section studied in depth.

### 4.2. Model verification

Rainfall was mainly concentrated along the southern foot of Borohoro Mountain during 12:00–18:00 UTC, June 16, 2016 (Fig. 5). Two rainfall centers, in Nilka County and Xinyuan County, experienced a maximum rainfall over 6 h of $> 48$ mm, the definition of a large rainstorm based on the Xinjiang Province local operational standard. There were two zonal precipitation belts distributed in Zhaosu County and the region between Changji and Urumqi. The model simulated the precipitation process well, with little deviation from the observations; for example, the simulated rainfall in Yining County was stronger than that observed, and the location of the simulated precipitation cell was to the northwest of the observed cell. The precipitation cell simulated in Nilka County was slightly weaker than that observed, and its location was to the north of the observed cell. Between 18:00 UTC, June 16 and 00:00 UTC, June 17, the rainfall along the Borohoro Mountains increased rapidly, and the precipitation cell was located

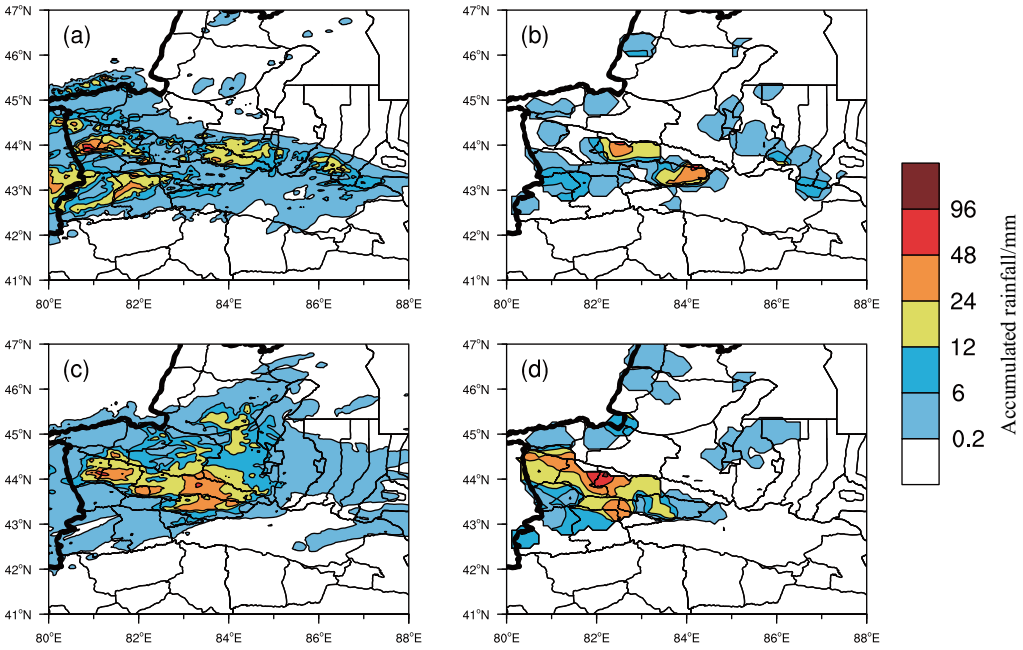



**Fig. 5.** The 6 h accumulated rainfall (mm) during (a), (b) 12:00–18:00 UTC, June 16, 2016 and (c), (d) between 18:00 UTC, June 16, 2016 and 00:00 UTC, June 17, 2016. (a), (c) simulation; (b), (d) observation.

in the western part of Nilka County, with a maximum rainfall of $>96$ mm occurring over 6 h. The precipitation zone was characterized by a clear zonal distribution along the Borohoro Mountains, with precipitation on the windward slope; the model reproduced the characteristics of the precipitation along the south foot of Borohoro Mountain well, except that three strong precipitation centers were observed, whereas only two precipitation centers appeared in the simulation.

There were differences in the precipitation intensity and location of precipitation cells between simulation and observation; however, overall, the precipitation areas and precipitation development trend were very similar. In other words, the model reproduced the precipitation process well, and the high-resolution model output was sufficiently accurate to analyze gravity wave characteristics during the torrential rainstorm.

## 5. Analysis of gravity waves

Gravity waves, particularly mesoscale IGWs, are typically closely correlated with rainstorms and other mesoscale weather systems. Therefore, we further examined the characteristics of gravity waves, the spatiotemporal evolution of gravity waves, and their roles during the rainstorm. We chose the cross-section indicated by the red line in Fig. 4 to conduct an in-depth spectral analysis. The cross-section region indicated by the red line in Fig. 4 represents the complex terrain in Xinjiang very well and is located in the rainfall area. The topography and convection are favorable to the generation of IGWs as shown above and, therefore, the cross-section may be an ideal zone to study the relationship between precipitation and IGWs.

### 5.1. Power spectrum analysis

We began by calculating the running average values of vertical velocity every 4 h, after which FFT was used to obtain the mean characteristics of the waves along the red line indicated in Fig. 4 between 12:00 UTC, June 16, 2016 and 12:00 UTC, June 17, 2016. A power spectrum analysis for different altitudes showed that wave signals were most prominent at an altitude of 19 km, with a clear single peak and narrow spectrum (Fig. 6). The wave numbers ranged from $-0.024$ km$^{-1}$ and $-0.009$ km$^{-1}$ (corresponding to horizontal wavelengths of 40–110 km) and the main wave frequencies varied from 0.0063 min$^{-1}$ to 0.02 min$^{-1}$ (corresponding to wave periods of 50–160 min) in the region of maximum wave energy density. These results indicate that the main wave signals were classic meso-$\beta$ scale waves with horizontal wavelengths of 40–110 km and periods of 50–160 min. The wave phase velocities were concentrated in the range of $-25$ m/s to $-10$ m/s, where the negative sign indicates that the waves were propagated in the westward direction.

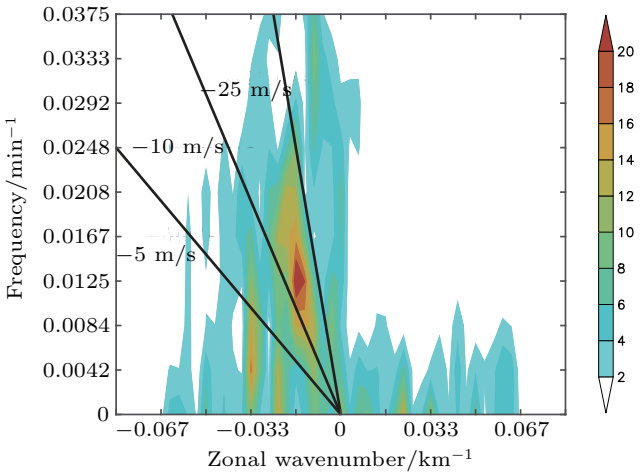



**Fig. 6.** Power spectrum density (m$^2$·s$^{-2}$) of the vertical velocity at an altitude of 19 km along the line shown in Fig. 4(a). Solid lines represent the wave phase velocities of $-5$ m/s, $-10$ m/s, and $-25$ m/s.

### 5.2. Cross-spectral analysis

A phase difference of 90° between the vertical vorticity and horizontal divergence was selected as the criterion to identify IGWs based on the polarization of gravity waves.[29] We calculated the phase spectrum and correlation spectrum of the vertical vorticity and the horizontal divergence using cross-spectral analysis to identify IGWs along the red line indicated in Fig. 4 during the rainstorm. For example, the phase

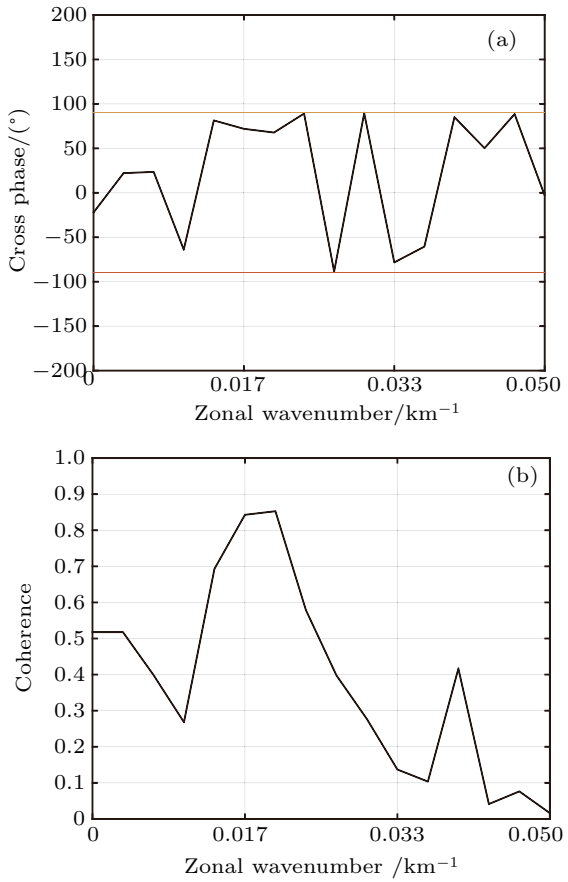



**Fig. 7.** (a) Phase spectrum and (b) correlation spectrum between the horizontal divergence and vertical vorticity at an altitude of 19 km at 11:00 UTC, June 17, 2016 along the line shown in Fig. 4(a).

spectrum and correlation spectrum of different wavenumbers calculated for 11:00 UTC, June 17, 2016 are presented in Fig. 7. The phase difference in the vertical vorticity and horizontal divergence with wavenumbers of 0.015–0.022 km$^{-1}$ and 0.033–0.036 km$^{-1}$ approached 90° (Fig. 7(a)). At the same time, the vertical vorticity and horizontal divergence had a high correlation coefficient, with values greater than 0.8 for waves with wave numbers of 0.016–0.020 km$^{-1}$ (Fig. 7(b)). Taken together, the waves with wavenumbers of 0.016–0.020 km$^{-1}$ (corresponding to horizontal wavelengths of 50–60 km) were identified as IGWs. IGWs with wavenumbers of 0.016–0.020 km$^{-1}$ were determined to be in the region of maximum wave energy density according to the power spectrum density analysis (Fig. 6), indicating that IGWs were the crucial waves in the torrential rainstorm.

### 5.3. Wavelet cross-spectral analysis

Based on the cross-spectral analysis, we were able to identify IGWs with detailed wavelengths and periods; however, the disadvantage of the cross-spectral analysis is that it could not be used to obtain the spatiotemporal characteristics of IGWs. Based on the phase spectrum, correlation spectrum, and amplitude spectrum of the vertical vorticity and horizontal divergence calculated using wavelet cross-spectral analysis, we obtained the spatiotemporal characteristics of IGWs along the red line indicated in Fig. 4. There was an extreme value in the 79.17–79.93°E, 81.10–81.45°E, and 81.50–82.00°E regions (Fig. 8(a)). The phase differences in vertical vorticity and horizontal divergence at 79.17–79.93°E and 80.69–82.21°E both approached 90°, particularly at 81.83–82.21°E, where the phase difference was exactly equal to 90° (Fig. 8(b)). There were three regions where the correlation coefficients were close to 0.9: near 79.55°E, near 80.5°E, and along 81.4–82.21°E, particularly along 81.83–82.21°E, where the correlation coefficients were exactly equal to 0.98 (Fig. 8(c)). There were clear gravity wave signals along 79.17–79.83°E, 81.35–81.45°E, and 81.5–81.83°E, particularly along 81.83–82.21°E where the correlation coefficients were close to 0.98 and the phase differences were exactly equal to 90°. Compared to the 1 h accumulated precipitation (Fig. 8(b)) along the cross-section line shown in Fig. 4, the region experiencing maximum rainfall corresponded well with the IGWs described above.

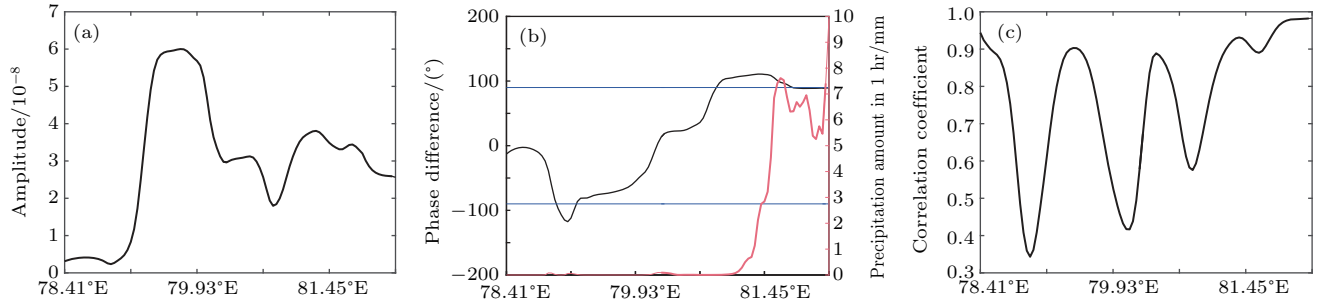



**Fig. 8.** (a) Wavelet amplitude spectrum, (b) phase spectrum, and (c) correlation spectrum between the horizontal divergence and vertical vorticity at an altitude of 19 km at 11:00 UTC, June 17, 2016 along the line shown in Fig. 4(a). Red line in panel (b) represents the 1-hour accumulated precipitation (mm).

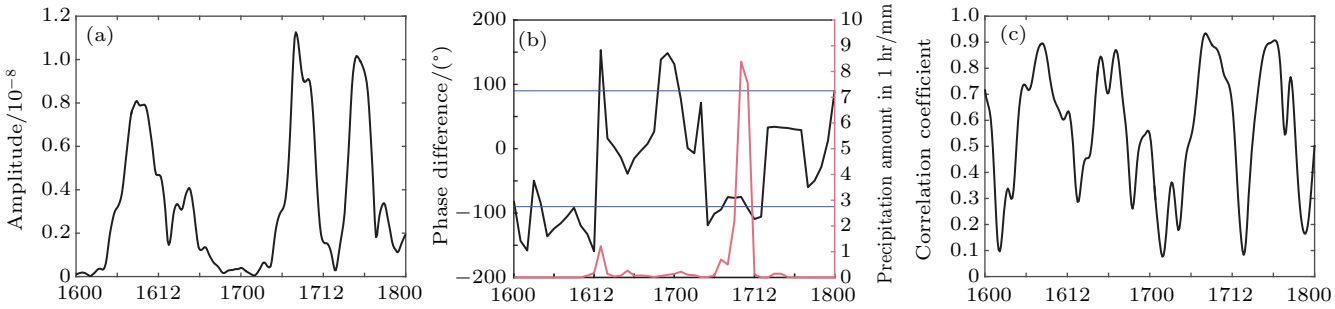



**Fig. 9.** (a) Wavelet amplitude spectrum, (b) phase spectrum, and (c) correlation spectrum between the horizontal divergence and vertical vorticity at an altitude of 19 km along 81.68°E. Red line in panel (b) represents the 1 h accumulated precipitation (mm).

To obtain the temporal characteristics of the IGWs in the rainstorm, we performed wavelet cross-spectral analysis of the vertical vorticity and horizontal divergence over time. Figure 9 shows the result of this analysis along 81.68°E at an altitude of 19 km between 00:00 UTC, June 16, 2016 and 00:00 UTC, June 18, 2016, where the horizontal axis is time in 10-min intervals. Between 06:00 and 12:00 UTC, June 17, 2016, there was an extreme value in the amplitude spectrum (Fig. 9(a)); the phase difference in vertical vorticity and horizontal divergence approached 90° (Fig. 9(b)) and the correlation coefficient exceeded 0.9 (Fig. 9(c)). This gives a clear IGW signal during that period. A precipitation peak appeared at 10:00 UTC, when the phase difference in the vertical vorticity and horizontal divergence approached 90° (Fig. 9(b)), indicating

that the precipitation peak and IGWs agreed well in time.

### 5.4. Reconstruction of gravity waves

According to our analysis of IGWs, we chose IGWs during the rainstorm with periods of 60–120 min, horizontal wavelengths of 50–60 km, and phase velocities of –10 m/s to –20 m/s for reconstruction by filtering the vertical velocity with the IFFT method. The westward propagation of gravity waves is clearly evident in Fig. 10(a). In three time periods (07:00–09:00 UTC, June 16; 13:00–14:00 UTC, June 16; and 09:00–14:00 UTC, June 17), the IGWs were clear, particularly during the period 09:00–14:00 UTC, June 17, when the IGW signal intensity along 80.4–82.21°E was strongest, corresponding well to our previous analysis. Precipitation was mainly concentrated along 80.4–82.21°E during 07:00–13:00 UTC, June 17 (Fig. 10(b)), with a precipitation peak at 11:00 UTC, June 17 near 81.4°E, corresponding well to the strongest waves shown in Fig. 10(a) and further revealing the close correlation between IGWs and rainstorms.

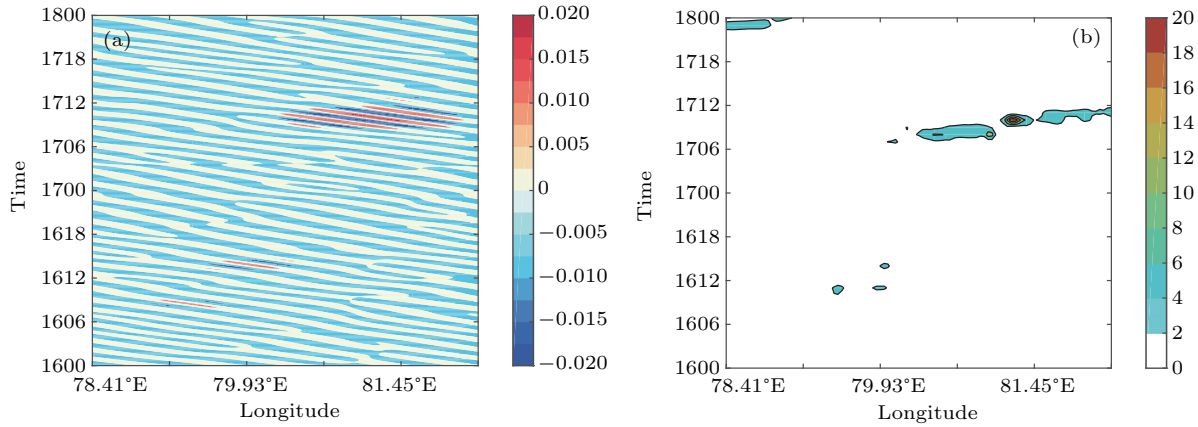



**Fig. 10.** (a) Time–longitude cross-section of reconstructed vertical velocity (m·s$^{-1}$) at an altitude of 19 km. Time on the $Y$-axis is formatted 'ddhh'. (b) Time–longitude cross-section of the 1 h accumulated precipitation (mm).

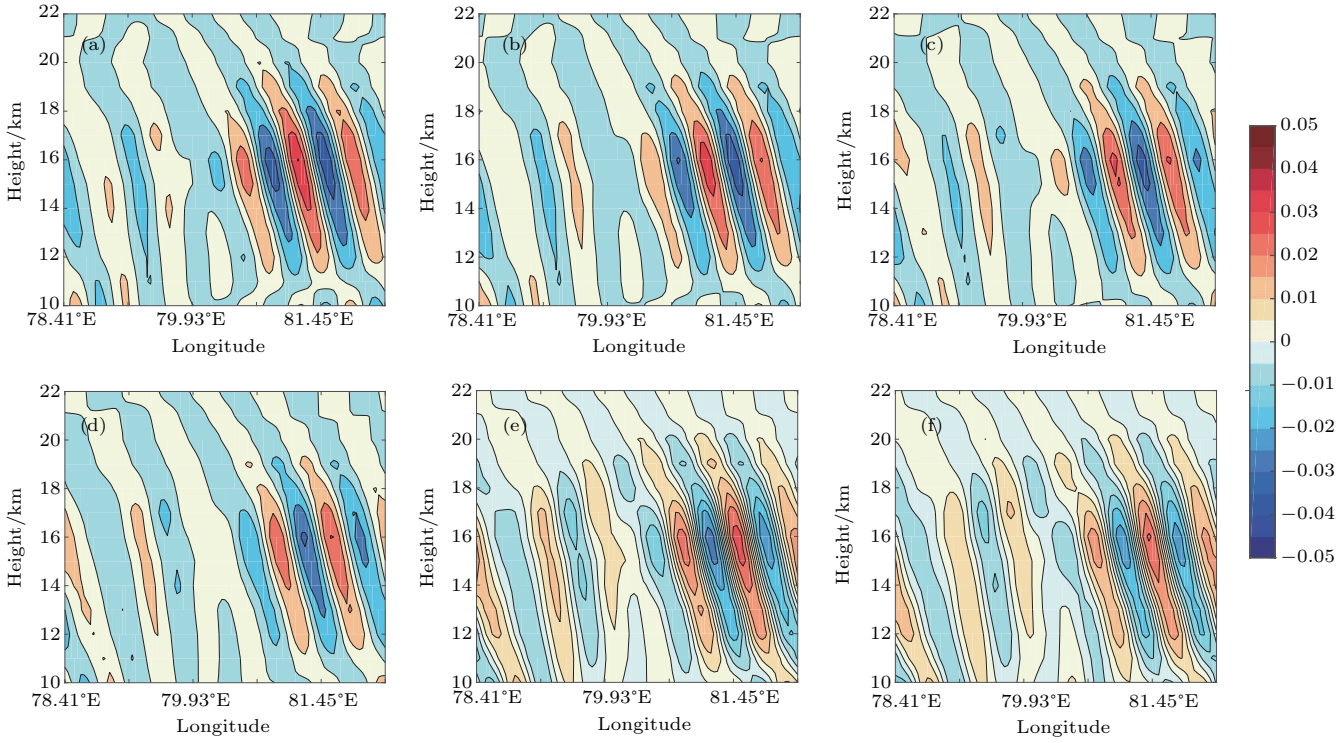



**Fig. 11.** Height–longitude cross-section of reconstructed vertical velocity (m·s$^{-1}$) at an elevation of 19 km from 10:40 UTC, June 17, 2016 to 11:30 UTC, June 17, 2016 calculated every 10 min. Selected horizontal wavelengths for reconstruction are 50–60 km, and periods are 60–120 min.

Figure 11 shows the reconstruction of the vertical velocity along the time-latitude cross-section. As shown in Fig. 11, gravity waves were active at a height of 12–20 km. Gravity waves propagated strongly westward during 10:40–11:30 UTC, June 17. A clear gravity wave signal was present along 80.69–82.21°E, which corresponded well to the precipitation signal shown in Fig. 10, again revealing correspondence between the gravity waves and the precipitation. While propa-

gating westwards, gravity waves along 80.69–82.21°E weakened gradually, with a limited intensity during 10:40–11:10 UTC, June 17; however, at 11:20 UTC, June 17, gravity waves suddenly became very weak, reflecting the transience of gravity wave characteristics. Gravity waves along 79.17–79.93°E enhanced with time from 11:30–11:40 UTC, June 17. Apart from the change in intensity of the gravity waves, the clearest trend was their upward propagation (Fig. 11).

## 6. Discussion and conclusion

This study focused on a torrential rainstorm event that occurred mainly in Yili Valley and along the Borohoro Mountains in Xinjiang Province, China. The trough was located to the west of Lake Balkhash at 500 hPa; the jet stream at 200 hPa provided favorable conditions for the development of the torrential rainstorm. Cyclonic circulation at 700 hPa and the unique topography in Yili Valley forced the airflow to converge and rise. The torrential rainstorm was characterized by heavy rainfall intensity, concentrated location, and spatial and temporal heterogeneity, indicating a typical mesoscale weather event. We simulated the development and occurrence of the torrential rainstorm using the WRF model, which successfully reproduced the precipitation area, intensity, and development trends during the rainstorm. Then we analyzed the characteristics of gravity waves during the rainstorm event using FFT and cross-spectral and wavelet cross-spectral analysis methods. The results showed that wave signals were prominent at an altitude of 19 km, with a clear single peak and a narrow spectrum. Waves at this altitude had horizontal wavelengths of 40–110 km and periods of 50–160 min. The wave phase velocities were concentrated within a range of −25 m/s to −10 m/s, and the waves propagated westwards.

Using cross-spectral analysis, we determined that the gravity waves were the crucial waves during the rainstorm. These gravity waves occurred mainly between 09:00 and 12:00 UTC, June 17, in the regions 79.17–79.93°E, 81.35–81.45°E, and 81.5–81.83°E. Wavelet cross-spectral analysis showed that gravity waves in the region 81.5–81.83°E were closely correlated with the 1 h accumulated precipitation, a possible rainstorm precursor for precipitation forecasting.

In conclusion, the comprehensive application of FFT and cross-spectral and wavelet cross-spectral analysis based on vertical velocity, horizontal divergence, and vertical vorticity could identify the signals of gravity waves, diagnose their parameters, and obtain the characteristics of their spatiotemporal evolution. The region and time experiencing extreme rainfall corresponded well with the IGWs described above. This spatiotemporal correspondence implies an interaction between the precipitation and IGWs and there may be a positive feedback mechanism between them to enforce and maintain the precipitation and IGWs during the rainstorm. Therefore, the use of these methods together may be helpful in numerical modeling and forecasting, and applying the knowledge of gravity waves to improve weather forecasts. We applied these methods for one case; further cases should be studied to examine and improve the methods and identify more potential rainstorm precursors. Avenues for future studies should include determining the mechanism of gravity wave generation during severe convection events, the role of the unique topography of Xinjiang, and the feedback of gravity waves to the mean flow.

## References


[1] Fritts D C and Alexander M J 2003 *Rev. Geophys.* **41** 1003
[2] Lilly D K and Kennedy P J 1973 *Journal of the Atmospheric Sciences* **30** 1135
[3] Uccellini L W and Koch S E 1987 *Monthly Weather Review* **115** 721
[4] Snyder C, Skamarock W C and Rotunno R 1993 *Journal of the Atmospheric Sciences* **50** 3194
[5] Kim Y H, Chun H Y, Park S H, Song I S and Choi H J 2016 *Atmospheric Chemistry and Physics* **16** 4799
[6] Wei J H and Zhang F Q 2014 *Journal of the Atmospheric Sciences* **71** 929
[7] Wei J H, Zhang F Q and Richter J H 2016 *Journal of the Atmospheric Sciences* **73** 3133
[8] Fritts D C 1984 *Journal of the Atmospheric Sciences* **41** 524
[9] Chimonas G and Hines C O 1986 *Journal of Geophysical Research-Atmospheres* **91** 1219
[10] Klostermeyer J 1990 *Radio Science* **25** 983
[11] Clark T L, Hauf T and Kuettner J P 1986 *Quarterly Journal of the Royal Meteorological Society* **112** 899
[12] Fovell R, Durran D and Holton J R 1992 *Journal of the Atmospheric Sciences* **49** 1427
[13] Piani C, Durran D, Alexander M J and Holton J R 2000 *Journal of the Atmospheric Sciences* **57** 3689
[14] Song I S, Chun H Y and Lane T P 2003 *Journal of the Atmospheric Sciences* **60** 1960
[15] Ran L K and Chen C S 2016 *Advances in Atmospheric Sciences* **33** 1271
[16] Lindzen R S 1974 *Journal of the Atmospheric Sciences* **31** 156
[17] Raymond D J 1987 *Journal of the Atmospheric Sciences* **44** 3528
[18] Nehrkorn T 1986 *Journal of the Atmospheric Sciences* **43** 2773
[19] Powers J G and Reed R J 1993 *Monthly Weather Review* **121** 2285
[20] Koch S E, Zhang F Q, Kaplan M L, Lin Y L, Weglarz R and Trexler C M 2001 *Monthly Weather Review* **129** 909
[21] Liu L, Ran L K and Sun X G 2015 *Advances in Atmospheric Sciences* **32** 1049
[22] Su T and Zhai G Q 2017 *Monthly Weather Review* **145** 335
[23] Thompson R O R Y 1978 *Quarterly Journal of the Royal Meteorological Society* **104** 691
[24] Cot C and Barat J 1986 *Journal of Geophysical Research-Atmospheres* **91** 2749
[25] Vincent R A and Fritts D C 1987 *Journal of the Atmospheric Sciences* **44** 748
[26] Lu C G, Koch S and Wang N 2005 *Journal of Geophysical Research-Atmospheres* **110** 01109
[27] Ge Z 2007 *Ann. Geophys.* **25** 2259
[28] Ge Z 2008 *Ann. Geophys.* **26** 3819
[29] Gao S T, Ran L K and Li X F 2015 *Fundamentals of Mesoscale Atmospheric Dynamics and Dynamic Prediction Methods for Rainstorms* (Beijing: China Meteorological Press) pp. 150–153 (in Chinese)